

pubs.acs.org/JACS Article

Efficient Redox-Neutral Photocatalytic Formate to Carbon Monoxide Conversion Enabled by Long-Range Hot Electron Transfer from Mn-Doped Quantum Dots

Connor Orrison, Jeremy R. Meeder, Bowen Zhang, Joseph Puthenpurayil, Michael B. Hall, Michael Nippe,* and Dong Hee Son*



Cite This: J. Am. Chem. Soc. 2021, 143, 10292-10300



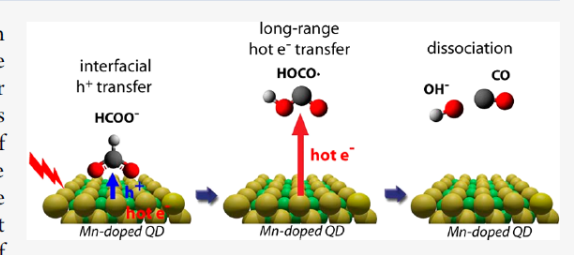
ACCESS I



Article Recommendations

s Supporting Information

ABSTRACT: Energetic hot electrons generated in Mn-doped quantum dots (QDs) via exciton-to-hot-electron upconversion possess long-range transfer capability. The long-range hot electron transfer allowed for superior efficiency in various photocatalytic reduction reactions compared to conventional QDs, which solely rely on the transfer of band edge electrons. Here we show that the synergistic action of the interfacial hole transfer to the initial reactant and subsequent long-range hot electron transfer to an intermediate species enables highly efficient redox-neutral photocatalytic reactions, thereby extending the benefits of



Mn-doped QDs beyond reduction reactions. The photocatalytic conversion of formate (HCOO⁻) to carbon monoxide (CO), which is an important route to obtain a key component of syngas from an abundant source, is an exemplary redox-neutral reaction that exhibits a drastic enhancement of catalytic efficiency by Mn-doped QDs. Mn-doped QDs increased the formate to CO conversion rate by 2 orders of magnitude compared to conventional QDs with high selectivity. Spectroscopic study of charge transfer processes and the computational study of reaction intermediates revealed the critical role of long-range hot electron transfer to an intermediate species lacking binding affinity to the QD surface for efficient CO production. Specifically, we find that the formate radical (HCOO)[•], formed after the initial hole transfer from the QD to HCOO⁻, undergoes isomerization to the (HOCO)[•] radical that subsequently is reduced to yield CO and OH⁻. Long-range hot electron transfer is particularly effective for reducing the nonbinding (HOCO)[•] radical, resulting in the large enhancement of CO production by overcoming the limitation of interfacial electron transfer.

■ INTRODUCTION

Hot electrons from semiconductor quantum dots (QDs) or plasmonic metal nanocrystals carrying excess kinetic energy have been shown to enhance various photochemical processes with great potential in photocatalysis 1-6 and photovoltaic applications.7-⁹ In particular, hot electrons produced via exciton-to-hot-electron upconversion in Mn-doped semiconductor QDs possess large excess energy with the average energy level of hot electrons reaching <1 eV below the vacuum level. 10 Hot electrons from Mn-doped QDs are several eV higher in energy than typical plasmonic hot electrons from metallic nanostructures. These energetic hot electrons from Mn-doped QDs can transfer across thick (>5 nm) insulating barriers^{7,11} and even produce hot electron photoemission under vacuum.¹² These illustrate a hot electron's unique capability to perform long-range transfer possibly extending beyond 5 nm and overcoming a high energy barrier. Recently, the long-range transfer of hot electrons from Mn-doped QDs has been shown to lead to superior performance during photocatalytic reduction reactions compared to conventional QDs, for which band edge electrons are limited to short-range interfacial electron transfer. For instance, hot electrons from Mn-doped QDs have been shown to increase the rate of photocatalytic H₂ production from water significantly compared to band edge electrons.¹³ They were also able to remove the requirement of close spatial proximity between a QD sensitizer and molecular catalysts in a hybrid photocatalyst system for the photocatalytic reduction of CO₂ to CO.³ While these studies demonstrated the benefits of long-range transfer of hot electrons from Mn-doped QDs for *photocatalytic reduction reactions*, the potential utilization to enhance *photocatalytic redox-neutral reactions* has remained unexplored.

Here, we report a new approach that extends the advantages of hot electrons from Mn-doped QDs beyond reduction reactions. Specifically, we show that redox-neutral reactions, in which the transfer of an electron to a nonbinding intermediate species on the QD surface generated by the initial hole transfer to the reactant, can maximally benefit from the long-range hot

Received: April 12, 2021 Published: June 30, 2021





electron transfer. For this purpose, we chose photocatalytic conversion of formic acid/formate to CO, which is an important reaction that produces a component of syngas from a feedstock that is highly abundant, being a common byproduct of industrial-scale organic syntheses and biomass processing. 14,15 Photocatalytic conversion of formic acid has previously been performed largely using metal oxides 16-19 and metal chalcogenides 15,20-22 as photocatalysts. Typically, the reaction products are mixtures of varying amounts of CO2, CO, and H2, depending on catalyst and reaction conditions, and result from two main competing pathways, i.e., dehydration (HCOOH \rightarrow CO + H₂O) and dehydrogenation (HCOOH \rightarrow CO₂ + H₂). Because of the relatively low efficiency of most photocatalysts, addition of a cocatalyst (e.g., Pt, CoCl₂)^{20,21} or sensitizable molecular catalyst (e.g., Fesalen)¹⁵ is often required to increase the catalytic efficiency. Although several earlier studies investigated the effect of varying cocatalyst and reaction conditions on the catalytic efficiency and product distribution, a detailed mechanistic understanding still remains elusive. 15,20,22

In this study, we show that sequential transfer of a hole and a hot electron by Mn-doped QDs during formate conversion, in which long-range hot electron transfer occurs to a transient intermediate species, drastically enhances CO production as compared to undoped QDs. Our comparative study shows that Mn-doped QDs allow for a 2 orders of magnitude higher CO production rate compared to undoped QDs, exhibiting a quantum yield of \sim 10%. In addition, CO constitutes 85% of the total product generated by Mn-doped QDs in contrast to undoped QDs, which produce H_2 as the major product with much lower efficiency. Based on combined spectroscopic and computational studies of the dynamics of charge transfer processes and structures of the likely reaction intermediates, we suggest a new mechanistic role of hot electrons for CO production from formate (Figure 1): the long-range transfer of

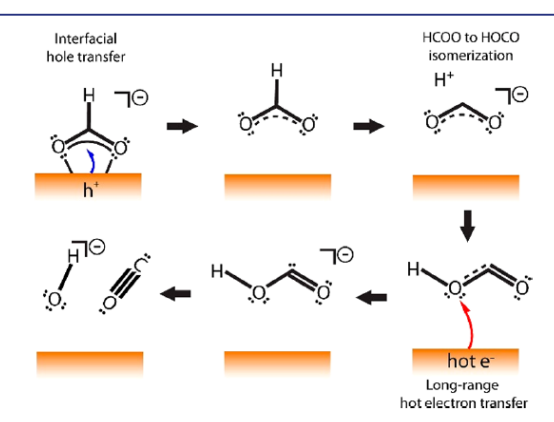


Figure 1. Illustration of the proposed formate to CO conversion mechanism via consecutive hole and hot electron transfer.

hot electrons from Mn-doped QDs to (HOCO)* radicals, which are formed by isomerization of the initial surface-bound formate oxidation product (HCOO)*. Since the (HOCO)* radical has a low binding affinity to the QD surface and is subject to diffusion away from the QD, the long-range hot electron transfer to (HOCO)* results in large enhancement in CO production efficiency. This study is the first demonstration of the effectiveness of hot electrons overcoming the shortcomings of the interfacial band edge electron transfer in a

multistep redox-neutral photocatalytic reaction requiring both electron and hole transfer. We expect a broader range of multistep photocatalytic reactions requiring the electron transfer to an intermediate species not bound to the catalyst surface can benefit greatly from the energetic hot electrons generated in Mn-doped QDs.

■ RESULTS AND DISCUSSION

Figure 2 shows the optical spectra and TEM images of Mndoped and undoped CdSSe/ZnS core/shell QDs used as the

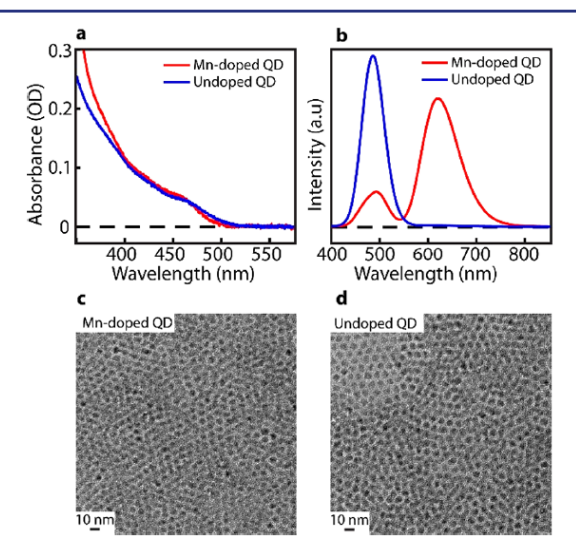


Figure 2. Absorption (a) and photoluminescence (b) spectra of Mndoped and undoped CdSSe/ZnS QDs. TEM images of Mn-doped (c) and undoped (d) CdSSe/ZnS QDs. Additional TEM images are in the Supporting Information.

source of both photogenerated electrons and holes required for the photocatalytic conversion of formate to CO. For comparison of the catalytic activities by hot electrons and band edge electrons, Mn-doped and undoped QDs sharing the same host structures were prepared. Both Mn-doped and undoped QDs have a nearly identical size and absorption coefficient at the excitation wavelength¹³ and therefore exhibit similar light-harvesting capability at the same QD concentration. The water-cooled photoreactor contained QDs, formic acid, and sodium hydroxide dissolved in deionized water with no additional cocatalyst or sacrificial charge scavenger. Among all the components in the reaction mixture, only the amount of sodium hydroxide was varied to examine changes of the photocatalytic activity at different pH values. A light-emitting diode (LED) emitting at 455 nm was used as the excitation source, which illuminated the entire reactor at the intensity of ~100 mW/cm². Detailed descriptions of the experimental conditions, variation of the experimental parameters, and detection method are in the Materials and Methods section.

A comparison of the amounts of CO and H₂ produced by Mn-doped and undoped QDs from aqueous formate solution at pH 12 in Figure 3 shows (i) a much higher (2 orders of magnitude) CO production for Mn-doped QDs and (ii) an inverted product selectivity with CO being the major product for Mn-doped QDs while undoped QDs produce mostly H₂. Under the reaction condition of Figure 3, H₂ and CO were the only gaseous products detected by gas chromatography (GC), and no CO₂ was detected in either case. Control experiments

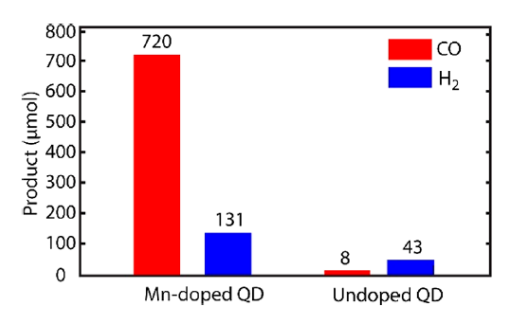


Figure 3. Amount of CO (red) and H2 (blue) produced by Mndoped QDs and undoped QDs after 2 h of illumination by a 455 nm emitting LED at pH 12.

performed in the absence of QD catalyst, formate, or light showed no CO production, indicating that QDs act as photocatalysts and that CO is indeed the product of photocatalytic formate conversion. In addition, we further confirmed that CO is derived from formate by detecting ¹³CO as the product when using ¹³C-labeled formate as the reactant (see Supporting Information).

Earlier studies of the hydrogen evolution reaction (HER) in water utilizing hot electrons from Mn-doped QDs had shown a 1 order of magnitude enhancement of HER efficiency as compared to undoped QDs. 13 For the photocatalytic CO₂ to CO reduction by the chemically nonlinked hybrid catalyst (Nicyclam)/QD system, a 6-fold enhancement of catalytic activity was observed for Mn-doped QDs as compared to undoped QDs.3 The enhanced activity exhibited by Mn-doped QDs was explained by long-range transfer of hot electrons to the reactant or molecular catalyst in addition to more favorable thermodynamics for reduction by hot electrons. The here observed 2 orders of magnitude enhancement for formate conversion to CO is much higher than the enhancement seen for HER and CO2 reduction. We consider that the benefit of hot electron transfer in enhancing the catalytic efficiency, and altering the reaction pathway (and product) is particularly significant when transient intermediate species that can diffuse away from the QD surface are involved in the electron transfer process, as will be discussed later. At pH 12, the quantum yield for CO and H₂ production under our experimental conditions is quite high, reaching 8.8% and 3.2%, respectively. (Details are in the Supporting Information.) We note that this catalytic efficiency is already obtained with nonoptimized Mn-doped QDs. We anticipate that further improvements can be made by optimizing the doping structure that determine the hot electron generation efficiency and the excitation condition that gains the most benefits of the superlinear dependence of hot electron generation via upconversion on light intensity.^{23,12}

To gain insight into the mechanism of efficient conversion of formate to CO, the photocatalytic efficiency and product composition were examined by varying several reaction conditions. First, we confirmed that both oxidation by a hole and reduction by an electron are required as the integral steps during formate to CO conversion. For this purpose, the change in CO and H₂ production in the presence of a sacrificial hole and electron scavenger was examined. Triethylamine (TEA), which is an effective hole scavenger for cadmium chalcogenide QDs, was added to the reaction mixture to investigate the effect of removing holes from the photoexcited QDs. Under the reaction condition of Figure 3 using Mn-doped QDs as the photocatalyst, the addition of TEA (0.77 M) suppressed CO

production by more than 97%. The addition of an electron scavenger²⁴ (methylene blue, 87 μ M) resulted in the decrease of CO production by 85% (see Table 1 for a summary of the

Table 1. Relative Amount of CO and H2 in the Presence of Electron and Hole Scavenger at pH 12 Referenced to the Case of No Added Scavenger

added charge scavenger	[CO] _{rel}	$[H_2]_{rel}$
none	1	1
TEA (0.77M)	0.026	0.67
methylene blue (87 μ M)	0.15	0.73

results). Since CO production decreases drastically in the presence of either electron or hole scavengers, rather than being enhanced by one type of scavenger, as has been observed for CO₂ reduction and HER in water, 3,13 transfer of both electron and hole to formate (or intermediates) is necessary during the formate to CO conversion process. It is interesting to note that the production of H₂ decreased only mildly by the same charge scavengers. This suggests that H2 is not derived from the same source as CO and is produced from an independent route such as the reduction of protons, as will be discussed further later. The same conclusion was inferred in earlier studies based on CO2 reduction with solvated electrons generated by H-terminated diamond and photocatalytic degradation of organic pollutants with CdS/ZnS core/shell nanoparticles. 25,26

Having established the necessity of both oxidation and reduction processes for formate to CO conversion, further experiments were performed to determine the nature of the initial charge transfer process. Although the decrease of PL intensity of the QDs after the addition of formate at pH 12 indicates the transfer of a charge carrier to formate, it does not tell which one is transferred initially. (See the Supporting Information.) For this reason, we employed pump-probe transient absorption measurements for the photoinduced charge transfer, which can distinguish which charge carrier is initially transferred from the QDs to the charge acceptor. In this measurement, the dynamics of the recovery of the exciton absorption bleach probed at the exciton absorption peak of the QDs (460 nm) following the pulsed excitation at 400 nm were compared in the presence and absence of formate in the aqueous dispersion of QDs. The dynamics of the bleach recovery in the QDs used in this study reflects the decay of the electron population, while it is not sensitive to the hole population due to the large difference in the degeneracy of the band edge electron and hole states.^{27,28} Therefore, the initial electron transfer from the QDs accelerates the bleach recovery while the initial hole transfer decelerates the bleach recovery due to the inhibited electron-hole recombination within the QDs, which are well understood from the earlier study.²

Figure 4 compares the bleach recovery dynamics probed at the peak of exciton absorption (460 nm) for the first 40 ps after the photoexcitation (400 nm) of the aqueous solution of Mn-doped and undoped QDs with and without formate at pH 11 (see Supporting Information for data in the nanosecond time window). For both Mn-doped and undoped QDs, the presence of formate slowed down the recovery of the bleach compared to when formate is absent, indicating that the holes are transferred initially. The generally faster recovery of the bleach in Mn-doped QDs compared to undoped QDs is due to exciton-Mn energy transfer that depletes both the electron

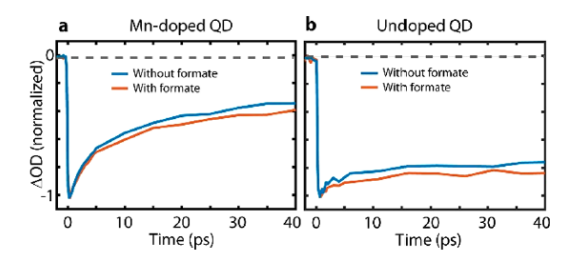


Figure 4. Transient absorption data pumped at 400 nm and probed at the exciton absorption peak (460 nm) of Mn-doped (a) and undoped (b) CdSSe/ZnS QDs with and without formate.

and hole population simultaneously, which is well known in Mn-doped QDs.²⁹ Since formate is known to adsorb on the surface of the metal chalcogenide QDs^{22,30} and the oxidation of formate by holes in the QDs is energetically favorable, the interfacial hole transfer to the surface-bound formate is likely the first event during formate to CO conversion.

Estimating the rate of hole transfer from the QDs to each formate ion from our present study is difficult due to insufficient information on the surface density of formate on the QDs. However, based on an earlier study that investigated hole trapping by surface-bound thiols on Mn-doped QDs, the rate of hole transfer by all adsorbed formate ions reflected in the deceleration of the bleach recovery in Figure 4 is on the order of 10^{10} s^{-1.29} It is notable that the extent of deceleration of the bleach recovery in the transient absorption data reflecting the efficiency of hole transfer is similar in both Mn-doped and undoped QDs. This indicates that the rate of the initial hole transfer process is similar in both Mn-doped and undoped QDs, consistent with the fact that hot carrier upconversion in Mn-doped QDs produces hot electrons rather than hot holes. Therefore, the subsequent charge transfer event, i.e., electron transfer, at the later stage of the reaction should be responsible for the observed differences in catalytic activities of Mn-doped and undoped QDs.

To gain additional mechanistic insights, the pH dependence of product formation was investigated using both Mn-doped and undoped QDs. Figure 5 shows the pH dependence of the amount of CO and H2 produced after 2 h of reaction within the pH range of 2-12, which is summarized in Table 2. A notable observation from Figure 5a is that the production of CO from Mn-doped QDs increases drastically by nearly 30 times between pH 10 and 12, while undoped QDs show consistently low CO production. This indicates that the enhancement of CO production gained by long-range hot electron transfer is effective only at high pH conditions. On the other hand, the production of H₂ shows a smaller increase (5fold) between pH 10 to 12 in Mn-doped QDs. The large difference in the increase of CO and H₂ production (30-fold vs 5-fold) upon the change of pH from 10 to 12 corroborates our earlier conclusion on CO and H2 being produced from different reactants, drawn from the analysis of the influence of electron and hole scavenger. Another notable observation is that CO₂ is detected in the product only at pH 4 and below. This is similar to the observation from the earlier photocatalytic and electrocatalytic studies using CdS QDs^{20,31} or a CdS electrode,³² although the proposed pathway of CO₂ production involves the oxidation of $(C\tilde{O}_2)^{\bullet-}$ by various different species.

The requirement of high pH for efficient CO production, a large difference in the dependences of CO and H₂ production

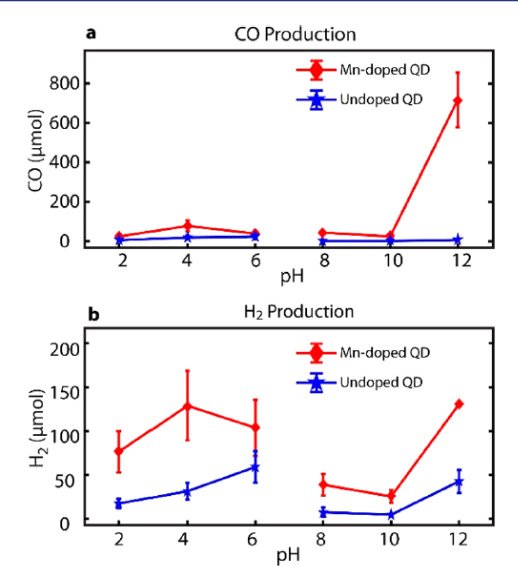


Figure 5. pH dependence of the amount of CO (a) and H₂ (b) produced after 2 h of reaction using Mn-doped and undoped QDs. For pH 8–12, CO and H₂ were quantified by using an internal standard for every run of the reaction. For pH 2–6, the error bar is higher since the internal standards were not used for every run.

on pH, and the presence of charge scavengers, and the absence of CO₂ production above pH 4 indicate that the reaction involves complex competitive kinetics and equilibria. Among others, the formic acid/formate equilibrium and the surface adsorption of formate competing with the native ligand (mercaptopropionic acid, MPA) on the QD surface are two important pH-dependent processes that can directly impact the photocatalytic reaction. Since the pK_a value of formic acid is 3.7, sufficient formate ions should be available well below pH 10. The sharp rise of CO production only above pH 10 can be understood from the thiol/thiolate equilibrium of MPA with a pK_a of >10 that competes with formate for the adsorption on the QD surface.³³ Since the bond between the sulfur of MPA and the QD surface becomes weaker with deprotonation of thiol, the rapid increase of CO production observed between pH 10 and 12 may be explained by the rapid shift of the surface adsorption equilibrium of formate. 34,35 Similarly, pHdependent protonation of reaction intermediates, such as the (HCO₂)• radical or (CO₂)• anion, will also be important in determining the final product. For instance, formation of CO₂ from the proton-electron transfer to (HCO₂)• will be facilitated at low pH, while it is increasingly unfavorable at high pH.

The above considerations are in good agreement with DFT calculations of the possible intermediate structures and their energies, which allow us to propose a mechanism for photocatalytic conversion of formate to CO by Mn-doped QDs. Figure 6 shows the conversion pathways of formate in aqueous medium at pH 12 to different sets of final products and the relative free energy of the reactants, products, and intermediates. Computational details are in the Materials and Methods section and in the Supporting Information. The initial step of the reaction is the interfacial hole transfer from the QDs to HCOO⁻ to generate the (HCOO)[•] radical. The calculated adiabatic ionization potential of HCOO⁻ (6.42 eV) in an aqueous environment is lower than the hole level in CdSSe/ZnS QDs used in this study (>6.7 eV below the

Table 2. pH Dependence of the Average Amount of CO and H₂ Produced after 2 h of Reaction Shown in Figure 5 and Quantum Yield (QY)^a

	Mn-doped QD				undoped QD			
pН	CO (µmol)	QY(CO) (%)	H ₂ (µmol)	QY(H ₂) (%)	CO (µmol)	QY(CO) (%)	H ₂ (µmol)	QY(H ₂) (%)
12	720	8.8	131	3.2	8	0.10	43	1.1
10	25	0.31	25	0.63	2	0.02	5	0.12
8	45	0.55	39	0.95	1	0.01	8	0.19
6	39	0.48	104	2.6	24	0.30	59	1.5
4	79	0.97	129	3.2	20	0.24	32	0.78
2	25	0.30	76	1.9	6	0.08	17	0.43

^aQY is defined as n(CO)/n(absorbed photon) and $2n(H_2)/n(absorbed photon)$ for CO and H₂, respectively, where n represents the number of molecules or photons.

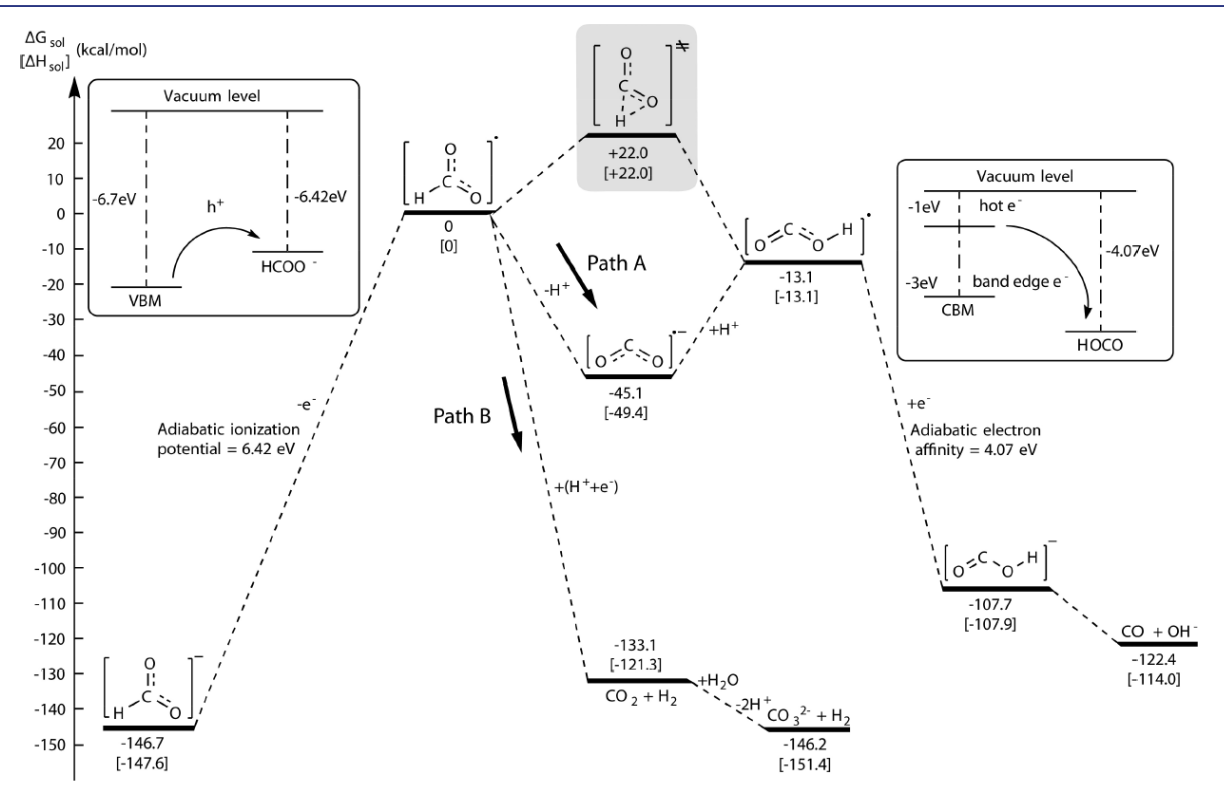


Figure 6. Energy profile for photocatalytic formate conversion with two possible sets of products. Relative Gibbs free energies in solvent (with the SMD solvation model) and enthalpies with solvent free energies [in square brackets] in kcal/mol are shown. The shading shows the transition state for the direct isomerization from $(HCOO)^{\bullet}$ to $(HOCO)^{\bullet}$. The Gibbs free energies of the chemical species that were involved in acid—base reactions (i.e., $(CO_2)^{\bullet -}$, CO_2+H_2 , and $CO_3^{2-}+H_2$) were calculated at pH = 12. VBM: valence band maximum, CBM: conduction band minimum.

vacuum level), consistent with the rapid initial hole transfer observed in transient absorption measurements.^{36,37} The high pH condition facilitates the adsorption of HCOO⁻ on the QD surface required for the efficient interfacial hole transfer as discussed above.

Following the hole transfer to form (HCOO), two competing reaction pathways are possible, i.e., paths A and B in Figure 6. Path B (dehydrogenation pathway) involves the protonation and one-electron reduction of (HCOO) either sequentially or concertedly to produce CO₂ and H₂. This pathway does not explain the observed dominant production of CO. While this path may not be kinetically favorable at high pH conditions, it may become more accessible at low pH and account for the production of CO₂ at pH 4 and below. In contrast, path A is the major pathway toward producing CO and is consistent with experimental observations. Here,

(HCOO) is first deprotonated to form (CO₂) and subsequently reprotonated to form (HOCO), an isomer of the initially formed (HCOO). (CO₂). is considered a common intermediate species present during the direct reduction of CO2 as well as the oxidation of formate under various electrocatalytic and photocatalytic reaction conditions. 15,20,25 Reduction of (HOCO) by hot electron produces HOCO-, which dissociates into CO and OH-. Although (HCOO) can directly isomerize to (HOCO) without going through the formation of $(CO_2)^{\bullet-}$, it is unlikely to be the case since it requires a transition state with significantly higher energy (22 kcal/mol; gray-shaded box in Figure 6.) In path A, the formation of HOCO⁻ from (CO₂)•- is considered the rate-determining step via (HOCO) as an intermediate species, while it is not clear whether sequential proton and electron transfer or concerted proton-coupled electron transfer

is the dominating process. In a recent Raman study of protonation of $CO_2^{\bullet-}$ in water, formation of $(HOCO)^{\bullet}$ in protonation/deprotonation equilibria with $(CO_2)^{\bullet-}$ was reported, ³⁸ supporting the proposed pathway of forming $(HOCO)^{\bullet}$ via protonation of $(CO_2)^{\bullet-}$ further. The protonation of $(CO_2)^{\bullet-}$ should be kinetically favorable since the proton is supplied directly from the prior deprotonation of $(HCOO)^{\bullet}$. The result from this Raman study also indicated that the alternative reaction of $(CO_2)^{\bullet-}$ with protons to produce CO_2 and H_2 suggested in an earlier study^{2.5} is less likely to occur under our experimental condition.

The electron transfer to (HOCO) with the calculated electron affinity of ~4.1 eV in aqueous media is the reaction step that is most strongly favored in the presence of hot electrons, ultimately leading to a large enhancement of the catalytic efficiency. The dissociation of HOCO- to CO and OH- was found to be barrierless according to our calculation. Since (HOCO) is charge neutral and features a protonated O atom, it will have much weaker binding affinity to the surface of QDs and may be formed further away from the QD surface, in contrast to formate undergoing interfacial hole transfer. In such a case, interfacial transfer of a band edge electron can be limited in reducing (HOCO) • even if its energy (~3 eV below the vacuum level 36,37) can provide sufficient thermodynamic driving force for the reduction of (HOCO). In contrast, hot electrons can provide not only a much larger thermodynamic driving force but also a large kinetic advantage via long-range electron transfer. Therefore, we attribute the 2 orders of magnitude enhancement in CO production gained by using Mn-doped QDs to the long-range transfer of energetic hot electrons to the transient intermediate species (HOCO), which cannot be readily reduced by short-range interfacial band edge electron transfer. The dominance of H2 as the major product when undoped QDs are used as the photocatalyst can also be explained by the preferential access of protons to the surface of the QD rather than (HOCO). One could view the difference in the spatial extent of the transfer of a hot electron and a band edge electron that alters the identity of the major electron-accepting species as the reason for the switching of the dominant product between Mn-doped and undoped QDs. It is interesting to compare our results with those from an earlier study of photocatalytic conversion of formate using undoped CdS QDs, where stripping of surface-capping ligands from the QD surface and replacement with charge-balancing BF₄⁻ counterions favored the production of CO in aqueous media.²⁰ While the reason for the switching in the product distribution and the underlying mechanism were not discussed, we conjecture that the absence of surface-capping ligands and the presence of BF₄-, capable of hydrogen bonding with protons,³⁹ may have allowed for preferential access of (HOCO) to the bare QD surface over protons.

Compared to the production of CO, H₂ production data in Figure 5b exhibit more complex pH dependence, showing a dip in the pH range of 8–10. This is likely because multiple pathways exist for H₂ production. Since formate itself is a hole acceptor, direct reduction of aqueous protons from the reaction medium is a likely pathway for H₂ production. Since the addition of a sacrificial hole scavenger (TEA) has a much weaker effect on H₂ production, in contrast to near complete quenching of CO production, the majority of produced H₂ is considered to be derived from the reduction of solvent protons. A significant increase of H₂ production between pH 10 and 12 is also consistent with the anticipated rapid increase

of the formate binding on the QD surface in the same pH range as discussed above. At low pH conditions (<pH 6), path B may be responsible for both CO_2 and H_2 . In the pH 2–6 range, both H_2 and CO_2 were produced in the largest quantity at pH 4. Two opposing effects of pH on the availability of formate and proton could be the reason for nonmonotonic pH dependence of CO_2 and H_2 production in this pH regime.

CONCLUSION

This work establishes the crucial role of long-range transfer of hot electrons from Mn-doped QDs to a transient intermediate species bearing weak binding affinity to the QD photocatalyst for highly effective photocatalytic conversion of formate to CO. This is the first report validating significant catalytic metric improvements by using long-range hot electron transfer from Mn-doped QDs beyond the reduction reactions, such as HER and CO₂ reduction, demonstrating the possible expansion of the applicability for a wider range of photocatalytic reactions. Specifically, the efficiency of redox-neutral conversion of formate to CO is improved by 2 orders of magnitude with high selectivity toward CO against H2 when Mn-doped QDs are used as the photocatalyst instead of the conventional QDs that do not produce hot electrons. In conjunction with experimental and computational studies, we propose a formate to CO conversion mechanism that involves interfacial formate oxidation by a hole, isomerization of an intermediate radical species, and reduction of a (HOCO)* radical by a hot electron, yielding CO and OH via barrierless dissociation. The mechanism strongly suggests that the large enhancement of CO production and selectivity for CO over H₂ by Mn-doped QDs are achieved by allowing for long-range hot electron transfer to the (HOCO) radical that may diffuse away from the QD surface and therefore is not effectively reduced by short-range interfacial electron transfer.

■ MATERIALS AND METHODS

Synthesis of QD Photocatalyst. Mn-doped and undoped CdSSe/ZnS core/shell QDs were prepared employing the previously reported synthesis procedure. 3,40 Initially, S and Se precursor solutions were prepared separately. For the S precursor solution, 0.081 g of sulfur powder was heated in 10 mL of octadecene (ODE) at 120 °C. For the Se precursor solution, 0.079 g of Se was dissolved in 1 mL of tert-butylphosphine (TBP). S and Se precursor solutions were mixed to prepare the final S/Se precursor solution. The core CdSSe QDs were prepared by injecting 2 mL of S/Se solution to Cd precursor solution prepared by dissolving 0.128 g of CdO in the mixture of 12 mL of ODE and 2 mL of oleic acid at 250 °C under a nitrogen atmosphere. After 100 s of reaction at 240 °C, the reaction was quenched via rapid cooling. The resultant core QDs were precipitated by centrifugation after adding acetone. Resuspension of the precipitate QD and precipitation was repeated three times to obtain purified core QDs. Addition of a ZnS shell to the core QDs was performed utilizing the successive ionic layer adsorption and reaction (SILAR) method. The core QDs dispersed in 6 mL of ODE and 2 mL of oleylamine were heated to 220 °C under a nitrogen atmosphere. The S precursor solution was added dropwise to the core QD solution over a period of 3 min and allowed to react for 10 min. Subsequently, the Zn precursor solution (0.25 M Zn stearate in anhydrous toluene with 5% octylamine) as added dropwise in the same manner. Dropwise addition of the S and Zn precursor solution was repeated to reach the desired thickness of the shell. For Mn doping, the purified core/shell QDs with two layers of ZnS shell were redispersed in 6 mL of ODE and 2 mL of oleylamine and heated to 220 °C. The Mn precursor solution was prepared by adding 0.029 g of Mn(OAc)₂ to 6 mL of oleylamine under nitrogen to avoid oxidation.

The Mn precursor solution was added dropwise and allowed to react for 20 min before cooling. Additional layers of ZnS shell were added to the purified Mn-doped QDs via the SILAR procedure described above to obtain the final Mn-doped QDs.

Ligand exchange of the resultant core/shell QDs was performed to make the QDs water-soluble. The original ligand (oleylamine) was replaced by mixing the QD solution (0.25 mL) dispersed in chloroform (2.5 mL) with the solution of MPA (0.15 mL) and NaOH (\sim 1.6 mL, 6 M) dissolved in the mixture of water (0.15 mL) and methanol (0.80 mL). After 3 h of stirring, the MPA-passivated QDs dispersed in the aqueous phase were recovered and purified by precipitation before use.

Quantification of Photodecomposition Product. The quantification of the photocatalytic product gases (CO and H₂) was performed using GC. The product gases for the analysis were collected by taking aliquots of the headspace from the sealed reactor vessel. The reactor with a total volume of 60 mL contained 1 mL of formic acid, 59 mL of deionized water, and QDs at a concentration of \sim 20 μ M. The pH of the solution was adjusted by adding NaOH. The reactor was then purged with Ar for 45 min and placed in a water bath. A 455 nm emitting LED was used for excitation, which illuminated the entire reactor at the intensity of 100 mW/cm². Aliquots of 200 µL were taken at 30 min intervals with a gastight syringe (gas syringe series A-2 Luer Lock 500 μL RN, VICI precision sampling) for the analysis of the concentration of the product gas. The analysis was performed on a GC with a thermal conductivity detector (for H2 detection) and flame ionization detector equipped with a methanizer (for CO detection). CH₄ was used as an internal standard to check the potential variation during the sampling and injection of the aliquots. The calibration of the detectors for the quantification of CO and H2 was done in the following way after the completion of each experiment. The reactor was first purged with Ar for 45 min to remove all CO, H2, and CH4. This was confirmed by taking a 200 μ L aliquot of the headspace in the reactor and injecting it into the GC for the analysis. The reactor was injected with the internal standard (200 µL of CH₄) and a known amount of CO and H_2 and allowed to equilibrate with the reactant mixture for 15 min. Subsequently, a 200 μ L aliquot of the headspace in the reactor was sampled and injected into the GC for the analysis. After adding an additional known amount of CO and H2 into the reactor, the sampling of the headspace and analysis with GC were repeated to complete the full calibration curve. The calibration curve was created from taking the ratio of the integrated areas between the internal standard and generated gases (CO:CH₄ and H₂:CH₄). For isotopic labeling studies, ¹³C-labeled formic acid (¹³C 99%, Cambridge Isotope Laboratories, Inc.) was used as the reactant, and the gaseous products were analyzed via GC-MS (Ultra GC/DSQ, ThermoElectron) to detect ¹³CO. Data from GC-MS confirming the detection of ¹³CO and further details are in the Supporting Information.

Transient Absorption Measurements. The transient absorption measurements were performed using a home-built pump-probe transient absorption spectrometer. The 400 nm pump beam was obtained by doubling the 800 nm output (80 fs, 3 kHz) of a titanium sapphire amplifier (KM Laboratories) with a 300 μm thick $\beta\text{-barium}$ borate crystal whose fluence was controlled by a linear polarizer and half-waveplate pair. The white light supercontinuum probe was generated by focusing a few microjoules of the 800 nm beam onto a 1 mm thick CaF2 window. A pair of amplified Si photodiodes were used with a monochromator (Newport, Oriel Cornerstone 130) and boxcar gated integrators to record the transient absorption data at the desired probe wavelengths. The desired probe wavelength was selected using a monochromator in front of the detector. The QD samples dispersed in water were circulated through a quartz flow cell (2 mm path length) to avoid any possible photodegradation or damage to the QDs from the photoexcitation. The concentration of the QDs was adjusted to obtain the absorbance of 0.4 or less in the flow cell. Sodium formate was added in the QD solution at the concentration of 1 M to examine the initial charge transfer process during the photocatalytic reaction.

Computational Details. Density functional theory (DFT) calculations of the intermediate species and their relative energy were carried out using Gaussian 16 Rev B01. All geometric optimizations and frequency calculations were performed with the B3LYP functional and the aug-cc-pVTZ basis sets. The implicit solvation model based on density (SMD) (water as dielectric) was applied to all species except for the gaseous molecules (H₂, CO₂, and CO). Gibbs free energies were standardized to 1 M for aqueous species and 1 atm for gas species at 298.15 K. All acid—base reactions were balanced with the H₂O/OH⁻ conjugate pair at pH 12 that matches the experimental condition for maximum CO production. Detailed tabulation of the optimized geometry and energy is in the Supporting Information.

ASSOCIATED CONTENT

Supporting Information

The Supporting Information is available free of charge at https://pubs.acs.org/doi/10.1021/jacs.1c03844.

Quantum yield calculation and additional details on the optimized geometries and energies from DFT calculations (PDF)

AUTHOR INFORMATION

Corresponding Authors

Dong Hee Son — Department of Chemistry, Texas A&M University, College Station, Texas 77843, United States; Center for Nanomedicine, Institute for Basic Science and Graduate Program of Nano Biomedical Engineering, Advanced Science Institute, Yonsei University, Seoul 03722, Republic of Korea; Ociclorg/0000-0001-9002-5188; Email: dhson@chem.tamu.edu

Michael Nippe — Department of Chemistry, Texas A&M University, College Station, Texas 77843, United States; orcid.org/0000-0003-1091-4677; Email: nippe@chem.tamu.edu

Authors

Connor Orrison — Department of Chemistry, Texas A&M University, College Station, Texas 77843, United States

Jeremy R. Meeder — Department of Chemistry, Texas A&M University, College Station, Texas 77843, United States

Bowen Zhang — Department of Chemistry, Texas A&M University, College Station, Texas 77843, United States

Joseph Puthenpurayil — Department of Chemistry, Texas A&M University, College Station, Texas 77843, United States; orcid.org/0000-0001-9910-9820

Michael B. Hall — Department of Chemistry, Texas A&M University, College Station, Texas 77843, United States; orcid.org/0000-0003-3263-3219

Complete contact information is available at: https://pubs.acs.org/10.1021/jacs.1c03844

Notes

The authors declare no competing financial interest.

ACKNOWLEDGMENTS

This work was supported by NSF (CBET-1804412, CHE-1664866) and the Welch Foundation (A-1880, A-0648) We thank Dr. Yohannes Rezenom for his assistance with conducting GC/MS measurements.

Article

- (1) Clavero, C. Plasmon-Induced Hot-Electron Generation at Nanoparticle/Metal-Oxide Interfaces for Photovoltaic and Photocatalytic Devices. *Nat. Photonics* **2014**, *8* (2), 95–103.
- (2) Mukherjee, S.; Libisch, F.; Large, N.; Neumann, O.; Brown, L. V.; Cheng, J.; Lassiter, J. B.; Carter, E. A.; Nordlander, P.; Halas, N. J. Hot Electrons Do the Impossible: Plasmon-Induced Dissociation of H₂ on Au. *Nano Lett.* **2013**, *13* (1), 240–247.
- (3) Parobek, D.; Meeder, J. R.; Puthenpurayil, J.; Nippe, M.; Son, D. H. Breaking the Short-Range Proximity Requirement in Quantum Dot/Molecular Catalyst Hybrids for CO₂ Reduction: Via Long-Range Hot Electron Sensitization. *J. Mater. Chem. A* **2020**, 8 (26), 12984–12989
- (4) Park, J. Y.; Kim, S. M.; Lee, H.; Nedrygailov, I. I. Hot-Electron-Mediated Surface Chemistry: Toward Electronic Control of Catalytic Activity. *Acc. Chem. Res.* **2015**, *48* (8), 2475–2483.
- (5) Zhang, Y.; He, S.; Guo, W.; Hu, Y.; Huang, J.; Mulcahy, J. R.; Wei, W. D. Surface-Plasmon-Driven Hot Electron Photochemistry. *Chem. Rev.* 2018, 118, 2927–2954.
- (6) Hou, B.; Shen, L.; Shi, H.; Kapadia, R.; Cronin, S. B. Hot Electron-Driven Photocatalytic Water Splitting. *Phys. Chem. Chem. Phys.* **2017**, *19* (4), 2877–2881.
- (7) Barrows, C. J.; Rinehart, J. D.; Nagaoka, H.; DeQuilettes, D. W.; Salvador, M.; Chen, J. I. L.; Ginger, D. S.; Gamelin, D. R. Electrical Detection of Quantum Dot Hot Electrons Generated via a Mn²⁺-Enhanced Auger Process. *J. Phys. Chem. Lett.* **2017**, 8 (1), 126–130.
- (8) Tang, H.; Chen, C. J.; Huang, Z.; Bright, J.; Meng, G.; Liu, R. S.; Wu, N. Plasmonic Hot Electrons for Sensing, Photodetection, and Solar Energy Applications: A Perspective. *J. Chem. Phys.* **2020**, *152* (22), 220901.
- (9) Goddeti, K. C.; Lee, C.; Lee, Y. K.; Park, J. Y. Three-Dimensional Hot Electron Photovoltaic Device with Vertically Aligned TiO₂ Nanotubes. *Sci. Rep.* **2018**, 8 (1), 7330.
- (10) Parobek, D.; Qiao, T.; Son, D. H. Energetic Hot Electrons from Exciton-to-Hot Electron Upconversion in Mn-Doped Semiconductor Nanocrystals. *J. Chem. Phys.* **2019**, *151*, 120901.
- (11) Dong, Y.; Rossi, D.; Parobek, D.; Son, D. H. Nonplasmonic Hot-Electron Photocurrents from Mn-Doped Quantum Dots in Photoelectrochemical Cells. *ChemPhysChem* **2016**, *17* (5), 660–664.
- (12) Dong, Y.; Parobek, D.; Rossi, D.; Son, D. H. Photoemission of Energetic Hot Electrons Produced via Up-Conversion in Doped Quantum Dots. *Nano Lett.* **2016**, *16* (11), 7270–7275.
- (13) Dong, Y.; Choi, J.; Jeong, H.-K.; Son, D. H.; Mcferrin, A. Hot Electrons Generated from Doped Quantum Dots via Upconversion of Excitons to Hot Charge Carriers for Enhanced Photocatalysis. *J. Am. Chem. Soc.* 2015, 137, 40.
- (14) Bozell, J. J. Connecting Biomass and Petroleum Processing with a Chemical Bridge. *Science* **2010**, 329, 522–523.
- (15) Irfan, R. M.; Wang, T.; Jiang, D.; Yue, Q.; Zhang, L.; Cao, H.; Pan, Y.; Du, P. Homogeneous Molecular Iron Catalysts for Direct Photocatalytic Conversion of Formic Acid to Syngas (CO+H₂). *Angew. Chem., Int. Ed.* **2020**, *59* (35), 14818–14824.
- (16) Wu, M.; Zhang, M.; Lv, T.; Guo, M.; Li, J.; Okonkwo, C. A.; Liu, Q.; Jia, L. The Effect of Calcination Atmosphere upon the Photocatalytic Performance of Au-La₂O₃/TiO₂ for Hydrogen Production from Formic Acid. *Appl. Catal., A* **2017**, 547, 96–104.
- (17) Mitoraj, D.; Beránek, R.; Kisch, H. Mechanism of Aerobic Visible Light Formic Acid Oxidation Catalyzed by Poly(Tri-s-Triazine) Modified Titania. *Photochem. Photobiol. Sci.* **2010**, 9 (1), 31–38.
- (18) Araña, J.; González Díaz, O.; Miranda Saracho, M.; Doa Rodríguez, J. M.; Herrera Melián, J. A.; Pérez Pea, J. Photocatalytic Degradation of Formic Acid Using Fe/TiO₂ Catalysts: The Role of Fe³⁺/Fe²⁺ Ions in the Degradation Mechanism. *Appl. Catal., B* **2001**, 32 (1–2), 49–61.
- (19) Mrowetz, M.; Selli, E. Photocatalytic Degradation of Formic and Benzoic Acids and Hydrogen Peroxide Evolution in TiO₂ and ZnO Water Suspensions. *J. Photochem. Photobiol., A* **2006**, *180* (1–2), 15–22.

- (20) Kuehnel, M. F.; Wakerley, D. W.; Orchard, K. L.; Reisner, E. Photocatalytic Formic Acid Conversion on CdS Nanocrystals with Controllable Selectivity for H₂ or CO. *Angew. Chem., Int. Ed.* **2015**, 54 (33), 9627–9631.
- (21) Nedoluzhko, A. I.; Shumilin, I. A.; Nikandrov, V. V. Coupled Action of Cadmium Metal and Hydrogenase in Formate Photodecomposition Sensitized by CdS. *J. Phys. Chem.* **1996**, *100* (44), 17544–17550.
- (22) Henglein, A.; Gutiérrez, M.; Fischer, C.-H. Photochemistry of Colloidal Metal Sulfides 6. Kinetics of Interfacial Reactions at ZnS-Particles. Berichte der Bunsengesellschaft für Phys. Chemie 1984, 88 (2), 170–175.
- (23) Chen, H. Y.; Maiti, S.; Son, D. H. Doping Location-Dependent Energy Transfer Dynamics in Mn-Doped CdS/ZnS Nanocrystals. ACS Nano 2012, 6 (1), 583–591.
- (24) Chen, H. Y.; Chen, T. Y.; Berdugo, E.; Park, Y.; Lovering, K.; Son, D. H. Hot Electrons from Consecutive Exciton Mn Energy Transfer in Mn-Doped Semiconductor Nanocrystals. *J. Phys. Chem. C* **2011**, *115* (23), 11407–11412.
- (25) Zhang, L.; Zhu, D.; Nathanson, G. M.; Hamers, R. J. Selective Photoelectrochemical Reduction of Aqueous CO₂ to CO by Solvated Electrons. *Angew. Chem., Int. Ed.* **2014**, 53 (37), 9746–9750.
- (26) Wang, X.; Peng, W. C.; Li, X. Y. Photocatalytic Hydrogen Generation with Simultaneous Organic Degradation by Composite CdS-ZnS Nanoparticles under Visible Light. *Int. J. Hydrogen Energy* **2014**, *39*, 13454–13461.
- (27) Klimov, V. I.; Schwarz, C. J.; Mc Branch, D. W.; Leatherdale, C. A.; Bawendi, M. G. Ultrafast Dynamics of Inter- and Intraband Transitions in Semiconductor Nanocrystals: Implications for Quantum-Dot Lasers. *Phys. Rev. B: Condens. Matter Mater. Phys.* 1999, 60 (4), R2177—R2180.
- (28) Knowles, K. E.; McArthur, E. A.; Weiss, E. A. A Multi-Timescale Map of Radiative and Nonradiative Decay Pathways for Excitons in CdSe Quantum Dots. *ACS Nano* **2011**, 5 (3), 2026–2035.
- (29) Maiti, S.; Chen, H. Y.; Park, Y.; Son, D. H. Evidence for the Ligand-Assisted Energy Transfer from Trapped Exciton to Dopant in Mn-Doped CdS/ZnS Semiconductor Nanocrystals. *J. Phys. Chem. C* **2014**, *118* (31), 18226–18232.
- (30) Rosson, T. E.; Claiborne, S. M.; McBride, J. R.; Stratton, B. S.; Rosenthal, S. J. Bright White Light Emission from Ultrasmall Cadmium Selenide Nanocrystals. *J. Am. Chem. Soc.* **2012**, *134* (19), 8006–8009.
- (31) Willner, I.; Goren, Z. Photodecomposition of Formic Acid by Cadmium Sulphide Semiconductor Particles. *J. Chem. Soc., Chem. Commun.* 1986, 5 (2), 172–173.
- (32) Feiner, A. S.; McEvoy, A. J.; Vlachopoulos, N.; Grätzel, M. Electrochemical Photooxidation of Carboxylates on CdS Electrodes. Berichte der Bunsengesellschaft für Phys. Chemie 1987, 91 (4), 399–402.
- (33) Danehy, J. P.; Noel, C. J. The Relative Nucleophilic Character of Several Mercaptans toward Ethylene Oxide. *J. Am. Chem. Soc.* **1960**, 82 (10), 2511–2515.
- (34) Green, M. The Nature of Quantum Dot Capping Ligands. J. Mater. Chem. 2010, 20, 5797–5809.
- (35) Lesiak, A.; Banski, M.; Halicka, K.; Cabaj, J.; Żak, A.; Podhorodecki, A. PH-Dependent Fluorescence of Thiol-Coated CdSe/CdS Quantum Dots in an Aqueous Phase. *Nanotechnology* **2021**, 32 (7), 075705.
- (36) Van de Walle, C. G.; Neugebauer, J. Universal Alignment of Hydrogen Levels in Semiconductors, Insulators and Solutions. *Nature* **2003**, 423 (6940), 626–628.
- (37) Smith, W. A.; Sharp, I. D.; Strandwitz, N. C.; Bisquert, J. Interfacial Band-Edge Energetics for Solar Fuels Production. *Energy Environ. Sci.* **2015**, *8*, 2851–2862.
- (38) Janik, I.; Tripathi, G. N. R. The Nature of the CO₂⁻ Radical Anion in Water. *J. Chem. Phys.* **2016**, 144 (15), 154307.
- (39) Grabowski, S. J. Hydrogen Bonds with BF₄⁻ Anion as a Proton Acceptor. *Crystals* **2020**, *10* (6), 460.

(40) Hsia, C. H.; Wuttig, A.; Yang, H. An Accessible Approach to Preparing Water-Soluble Mn²⁺-Doped (CdSSe)ZnS (Core)Shell Nanocrystals for Ratiometric Temperature Sensing. *ACS Nano* **2011**, *5* (12), 9511–9522.